

Statistical mechanics for organic mixed conductors: phase transitions in a lattice gas

Lukas M. Bongartz

Institute for Applied Physics, Technische Universität Dresden, 01187 Dresden, Germany

Organic mixed conductors (OMCs) represent a promising class of materials for applications in bioelectronics, physical computing, and thermoelectrics. Rather unparalleled, OMCs feature dynamics spanning multiple length and time scales, involving an intricate coupling between electronic, ionic, and mass transport. These characteristics set them notably apart from traditional semiconductors and hinder the description by conventional semiconductor theory. In this work, we approach the charge carrier modulation of OMCs using statistical mechanics. We discuss OMCs from a first-principles perspective and contrast them with established semiconductor materials, highlighting key differences in their collective charge carrier dynamics. This motivates our toy model describing OMCs as a lattice gas, which we analyze within the grand canonical ensemble. The model exhibits a first-order phase transition analogous to a classical vapor–liquid transition, governed by temperature and chemical potential. In doing so, it explains the formation of distinct low- and high-density carrier phases – a mesoscale phenomenon recently observed experimentally. It also demonstrates how metastability near the phase boundary can give rise to history-dependent characteristics in device operation, a similarly well-reported effect in OMC transistors. This work is intended as a simple motivation for studying OMCs through the lens of statistical mechanics, offering a more natural description than traditional semiconductor models developed for materials of fundamentally distinct character.

I. INTRODUCTION

Organic mixed conductors (OMCs) – semiconducting polymers that allow for both ion and electron transport – represent a novel class of electronic materials, distinct from conventional inorganic systems like silicon [1]. While traditional semiconductors are generally operated (switched between conductive and non-conductive states) using the field effect, OMCs are controlled electrochemically. In this mode, the dynamic introduction and retrieval of dopants into the semiconductor become a central part of device operation, as opposed to the singular introduction of dopants during fabrication in legacy systems.

While OMC technology is still in its infancy and fundamental research stage, it is beginning to crystallize as a promising candidate to complement application layers inaccessible to silicon et al. These include, in particular, bioelectronics such as neural interfaces and bio-inspired computing [2]. The archetypal OMC device is the organic electrochemical transistor (OECT) [3]. In this device architecture, the semiconductor channel is coupled to a gate electrode via an electrolyte. The electrolyte acts as an ion reservoir, donating dopants into the polymer semiconductor mesh, where they compensate the (n- or p-type) electronic charge carriers hosted within the OMC’s π -system. As in conventional transistor devices, source and drain contacts probe the channel conductivity in terms of a drain current, with the key difference that carriers are driven throughout the entire volume of the channel, rather than being confined to the surface. We want to stress that OMCs represent one of the most diverse materials classes developed to date, where minor modifications in the molecular structure or material processing can manifest in profound differences on the microscale (e.g., morphology, carrier mobility, mass and charge ca-

pacity) [4]. We here take a holistic view on OMCs, intentionally abstracting away from microscopic details to focus on the general characteristics of charge carrier dynamics. We thus consider generalized model systems of both silicon-like and carbon-based polymer semiconductors. This viewpoint already allows us to identify several key distinctions between the physics governing each.

Most notably, OMC operation features extremely high charge carrier densities ($\sim 10^{20}$ – 10^{21} cm^{-3}), orders of magnitude beyond what is typical in inorganic semiconductors and approaching a 1:1 population of electronic charges on the molecular hosting sites [5–7]. Due to the disordered morphology, charge transport is often of a hopping nature, rather than band-like [8–10]. As carbon-based systems, OMCs also feature low dielectric constants [11, 12], which amplify both Coulomb and higher-order multipole interactions. While the electrolytic environment partially screens long-range Coulomb interactions (Debye screening), short-range correlations remain significant. A simple order-of-magnitude estimate using archetypal material parameters (Appendix A) suggests that carrier–carrier coupling in OMCs exceeds that in silicon-based systems by several $k_B T$, across the entire regime of relevant carrier densities (10^{16} – 10^{19} cm^{-3} for silicon; 10^{18} – 10^{21} cm^{-3} for OMCs). This has important consequences for charge carrier dynamics, causing deviations from standard frameworks such as Miller–Abrahams hopping transport [13].

Here, we focus on the charge carrier density and its modulation by an external bias, while leaving the incorporation of transport phenomena for a follow-up publication. Several works have shown the impact of particle interactions in OMC operation, such as electron–electron [6, 14], electron–phonon [15], and electron–dopant modes [6, 16, 17]. Collectively, these give rise to a dynamic density of states that evolves with the carrier density

itself and contribute to a heterogeneous doping process. They reveal an intricate configurational landscape involving the coupling between electronic charge carriers, mobile ionic dopants, molecular vibrations, and morphology. Two recent reports on an established OMC serve as an illustrative case study: Wu et al. provided direct experimental evidence that an electrochemically doped OMC forms ~ 10 nm domains of distinct electronic character, whose growth is consistent with Model-B-type coarsening [18, 19]. This non-equilibrium phase separation is tied to a strong coupling between carrier populations and structural rearrangements, linking it to Cahn–Hilliard–like dynamics at the mesoscale [20]. Using the same OMC with a strongly interacting electrolyte, Bongartz et al. demonstrated OECTs with persistent hysteresis on experimental timescales, thermodynamically ascribed to a phase separation into domains of high and low doping degree [21].

These observations converge on a common underlying theme: a non-uniform stabilization of charge carriers, which suggests a connection to our coupling estimates in Appendix A. In inorganic semiconductors like silicon, charge carriers remain strongly delocalized, weakly interacting, and efficiently screened by fast electronic polarization, which suppresses correlation effects. This leads to the well-known description as a quasi-free electron gas governed by effective-mass physics. In polymer semiconductors, the situation is fundamentally different: while mobile ions in the electrolytic environment effectively screen long-range Coulomb repulsion, strong electron–phonon coupling leads to polaron formation and lattice-mediated attractive interactions that are not present in conventional semiconductors. Combined with near-unity site occupations at high doping levels, configurational entropy becomes central to the carrier distribution. This regime lies outside the scope of traditional semiconductor theory, which takes the weakly interacting electron gas as its foundation.

Herein, we take the carrier gas picture at face value. Using statistical mechanics, we treat the population of charge carriers within the grand canonical ensemble of a lattice gas, which naturally accommodates collective and critical phenomena. Two driving forces, the energetic interactions between carriers and configurational entropy, compete in controlling the degree of carrier aggregation. The emergence of phase-separated domains and hysteretic bistability can then be understood in analogy to a collective vapor–liquid phase transition. We proceed as follows: We first review the lattice gas in terms of its microscopic states and interactions, before exploring its equilibrium and dynamical behavior through Monte Carlo simulations. Using mean-field analysis, we formalize the grand canonical probability distribution and close by connecting this statistical picture to experimental observables in transistor operation.

II. MAIN

A. The lattice gas model

Distributing charge carriers across the available sites in an OMC gives rise to a vast number of possible configurations, known as microstates. Meanwhile, device operation probes macroscopic properties, such as the total channel conductivity or impedance, which represent ensemble averages over this microscopic landscape. This separation of scales motivates a statistical treatment of the system’s equilibrium properties. We focus on the subsystem responsible for the drain current: localized electronic charge carriers strongly coupled to local lattice distortions. This subsystem can be effectively decoupled from the bulk material by a separation of timescales between mobile carriers and large-scale structural rearrangements. We thus treat the molecular backbone as a quasi-static grid of sites hosting the carrier population. Coarse-graining into a lattice, each site represents a mesoscopic region of the polymer, for which we here consider a binary occupation encoded by $n_i \in \{0, 1\}$. This picture maps onto a lattice-gas model, mathematically equivalent to the Ising model, which we use as a deliberately simple toy framework to isolate and study the role of carrier–carrier interactions.

Charge carriers in conjugated polymers are not free electrons but quasi-particles often referred to as polarons, where the electronic charge is strongly coupled to local, fast vibrations of the molecular lattice [22]. Rather than being point-like, the electronic charge is delocalized over several repeat units (intra- and interchain), which reduces the Coulomb self-energy and can lead to sizable dipole moments and polarizability. In coupling to the lattice relaxation, it deepens the associated potential well and, for sufficiently strong electron–phonon coupling, can make it energetically favorable for a second carrier to occupy the same region. As estimated in Appendix A, these cooperative, short-range effects can outweigh the residual like-charge repulsion, motivating our central assumption of a net effective attraction between charge carriers. This energetic stabilization is analogous, in spirit, to the attractive part of intermolecular potentials (e.g., Lennard–Jones) that drives the condensation of classical fluids from a vapor. We stress that the heterogeneous environment in OMCs implies that polaronic carriers are not identical but exhibit a distribution in spatial extent, energy, and coupling strength. This notion may be captured by the concept of ‘weighted polarons,’ which we neglect here for simplicity.

In operation, an OMC is not an isolated system; it is in contact with a thermal environment (the ‘heat bath’) and a reservoir of dopant ions (the electrolyte). By the separation of timescales, the number of molecular host sites constitutes a constant effective volume (V) for the electronic subsystem. The exchange of energy with the heat bath is governed by the temperature (T), while the exchange of particles (charge carriers) with the reservoir

is governed by the chemical potential (μ). This perspective, allowing for particle exchange within a fixed effective volume, naturally leads to the grand canonical ensemble. For a microstate X with $N(X) = \sum_i n_i$ carriers, the probability follows the Boltzmann distribution:

$$\mathbb{P}[X] \propto \exp\left(-\frac{E(X) - \mu N(X)}{k_B T}\right), \quad (1)$$

where $E(X)$ is the internal energy of the microstate and $N(X) = \sum_i n_i$ is the total number of carriers. For simplicity, we set $k_B = 1$ henceforth. $E(X)$ is defined by the Hamiltonian for our lattice gas:

$$H[X] = -J_0 \sum_{\langle i,j \rangle} n_i n_j, \quad (2)$$

where $J_0 > 0$ is the microscopic attractive interaction energy between nearest-neighbor carriers motivated previously. We interpret μ as a fixed reservoir parameter (control parameter) and will later connect it to the electrochemical potential in device operation.

While the probability of a single microstate may be known, the probability of an observable macrostate (e.g., one with a specific carrier density $\rho = N/V$) must also account for its degeneracy, that is, the total number of microstates, Ω , that may realize it. The probability of such a macrostate is proportional to the Boltzmann factor weighted by this degeneracy: $\mathbb{P}(\text{macrostate}) \propto \Omega \cdot e^{-(E-\mu N)/T}$. This degeneracy is quantified by the configurational entropy, $S = \ln \Omega$. Substituting into the probability expression reveals the central role of the thermodynamic potential:

$$\mathbb{P}(\text{macrostate}) \propto e^S e^{-(E-\mu N)/T} = e^{-\Phi/T}, \quad (3)$$

where the grand potential is defined as $\Phi = E - TS - \mu N = F - \mu N$, with $F = E - TS$ being the Helmholtz free energy. The system's equilibrium state is the one that maximizes this probability, i.e., which minimizes Φ . This setup represents the fundamental thermodynamic balance between the energetic drive for ‘organization’ (minimizing E), the entropic drive for ‘chaos’ (maximizing S), and the coupling to the particle reservoir ($-\mu N$).

B. Monte Carlo simulation

We investigate this model using Markov chain Monte Carlo (MCMC) simulations based on Metropolis acceptance [23], sampling from the grand canonical ensemble. The algorithm (Alg. 1) repeatedly attempts to change the state of a randomly selected lattice site. A proposed flip (e.g., creating a carrier at an empty site) results in a change in the system’s energy and particle number, ΔE and ΔN . The move is accepted with probability $P_{\text{accept}} = \min(1, e^{-(\Delta E - \mu \Delta N)/T})$, thus satisfying detailed balance with respect to the grand canonical distribution

Algorithm 1: Grand-canonical MCMC

```

Require:  $L, T, \mu, J_0, N_{\text{sw}}$ 
1: Initialize  $\{n_i\}$  with  $n_i \sim \text{Bernoulli}(\rho_0)$ 
2: for  $s = 1$  to  $N_{\text{sw}}$  do
3:   for  $k = 1$  to  $L^2$  do
4:     Pick site  $i$  uniformly at random
5:      $h_i \leftarrow \sum_{j \in \mathcal{N}(i)} n_j$  {neighbor count}
6:      $\Delta N \leftarrow 1 - 2n_i$ 
7:      $\Delta E \leftarrow -J_0 \Delta N h_i$ 
8:      $\Delta H \leftarrow \Delta E - \mu \Delta N \{\Delta(E - \mu N)\}$ 
9:      $P_{\text{acc}} \leftarrow \min(1, e^{-\Delta H/T})$ 
10:    if  $U \sim \text{Uniform}(0, 1) < P_{\text{acc}}$  then
11:       $n_i \leftarrow 1 - n_i$ 
12:    end if
13:   end for
14: end for

```

and ensuring that the simulation converges to the system’s equilibrium state at fixed μ and T . We provide a simulation tool under [24].

We run the simulation across a grid of parameters (T, μ) and map the system’s equilibrium behavior. The result is the phase diagram shown in Fig. 1, which plots the equilibrium charge carrier density ρ as a function of temperature and chemical potential. The diagram reveals two distinct regimes. At high temperatures, the carrier density changes smoothly and continuously with μ , analogous to a supercritical fluid. At low temperatures, a discontinuous jump appears in the density at a critical chemical potential $\mu_c = -J$ (Appendix B). This is a first-order phase transition, separating a low-density “vapor” phase of largely independent carriers from a high-density “liquid” phase of correlated, stabilized carriers. Near this phase transition line, the system

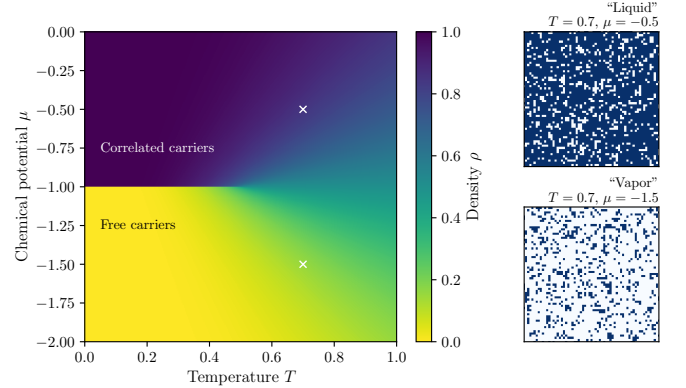


FIG. 1. Phase diagram of a lattice gas model, mapping equilibrium charge carrier density ρ against temperature T and chemical potential μ ($J = 1.0$). At high temperatures, density varies smoothly (supercritical fluid). At low temperatures, a sharp, first-order phase transition occurs at $\mu_c = -J$, dividing a low-density “vapor” phase (free carriers) from a high-density “liquid” phase (correlated carriers). Insets show simulation snapshots for each phase, corresponding to the markers in the phase diagram.

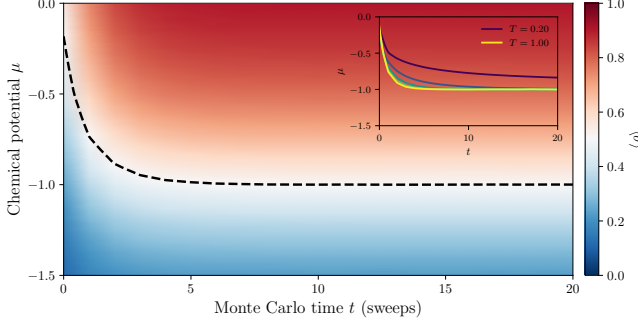


FIG. 2. Dynamical phase diagram showing the average carrier density $\langle \rho \rangle$ as a function of Monte Carlo time t and chemical potential μ at fixed temperature $T = 0.8$ ($J = 1.0$, $\rho_0 = 0$, averaged over 10^3 realizations). The dashed line marks $\langle \rho \rangle = 0.5$, indicating the dynamical phase boundary. Inset: the $\langle \rho \rangle = 0.5$ contour for temperatures $T = 0.2$ (blue) to $T = 1.0$ (yellow), showing that metastable states become increasingly long-lived at lower temperatures.

exhibits metastability; if parameters are changed such that a new phase becomes favorable, the system can remain trapped in the previous macrostate for an extended period of time, as an energy barrier for nucleation of the new phase must be overcome.

For illustration, we show a dynamical phase diagram at fixed temperature in Fig. 2. The system is initialized in an empty state ($\rho_0 = 0$), and independent simulations are performed at different values of the chemical potential μ , each evolving at fixed thermodynamic parameters. The color map shows the average density $\langle \rho \rangle$ as a function of Monte Carlo time t and chemical potential μ . The dashed line marks the dynamical phase boundary at $\langle \rho \rangle = 0.5$. At short times, this boundary is displaced from the equilibrium coexistence value $\mu_c = -J$; the system remains in its initial low-density state even when the high-density phase is thermodynamically favored. As $t \rightarrow \infty$, the boundary converges to μ_c , recovering the equilibrium prediction. The inset shows how this convergence slows at lower temperatures, revealing increasingly long-lived metastable states as thermal fluctuations weaken.

We note that the specific shape of the dynamical boundary depends on the choice of sampling algorithm. This toy model uses Metropolis acceptance, where each Monte Carlo sweep can be interpreted as a Poisson process with transition rates set by the acceptance probability (line 9 of Alg. 1). An alternative is Kawasaki dynamics, where pairs of neighboring sites exchange occupation rather than flip individually, conserving total particle number and mimicking diffusive hopping.

C. Mean-field analysis

The regular square lattice in our simulation represents a significant idealization. Real OMCs are high-entropy

materials whose long-chain polymers possess vast conformational degrees of freedom, resulting in substantial structural heterogeneity. While OMC microstructures can comprise mixtures of (semi-)crystalline and amorphous regions, a coarse-grained model can describe the collective system properties through the average interaction experienced by carriers, rather than through specific local geometric arrangements. To this end, we relax all geometrical constraints by adopting a mean-field approximation, effectively treating the system as a fully connected network.

The interaction energy of a given state depends only on the total number of carriers, $N(X)$, not their specific arrangement. For a system with V total sites, this leads to the coarse-grained interaction energy

$$E(X) = -\frac{J}{V} N(X)^2, \quad (4)$$

where J is the effective mean-field coupling that encapsulates the underlying microscopic interactions (Appendix B). Substituting this expression into the grand canonical Boltzmann distribution gives

$$\mathbb{P}[X] \propto \exp\left(\frac{J}{TV} N(X)^2 + \frac{\mu}{T} N(X)\right). \quad (5)$$

This formulation connects the probability of a single microstate to its macroscopic density $\rho(X) = N(X)/V$. To find the probability of observing a macrostate with a given density ρ , we must multiply by the number of ways to arrange $N = \rho V$ carriers on V sites. This combinatorial factor gives rise to the system's entropy. A standard derivation using Stirling's approximation (Appendix C) allows us to write the probability distribution for the density ρ as

$$\mathbb{P}[\rho] \propto \exp\left(V \left[\frac{J\rho^2 + \mu\rho}{T} - (\rho \ln \rho + (1-\rho) \ln(1-\rho)) \right]\right). \quad (6)$$

For a large system ($V \gg 1$), the probability distribution is sharply peaked around the density ρ^* that maximizes the term in the exponent. We can identify this exponent (per unit volume) as $-\phi_{T,\mu}(\rho)/T$, where

$$\phi_{T,\mu}(\rho) = f(\rho) - \mu\rho \quad (7)$$

is the mean-field grand potential density, with

$$f(\rho) = -J\rho^2 + T[\rho \ln \rho + (1-\rho) \ln(1-\rho)] \quad (8)$$

being the Helmholtz free energy density. The relationship between the probability and the grand potential landscape is visualized in Fig. 3. The peaks in the probability distribution $\mathbb{P}[\rho]$ correspond to minima in the grand potential density $\phi_{T,\mu}(\rho)$, which represent stable or metastable equilibrium states. At a temperature below the critical point, the landscape is non-convex and exhibits two minima corresponding to low- and high-density phases. The chemical potential controls the relative depth of these minima: for $\mu < \mu_c$, the low-density

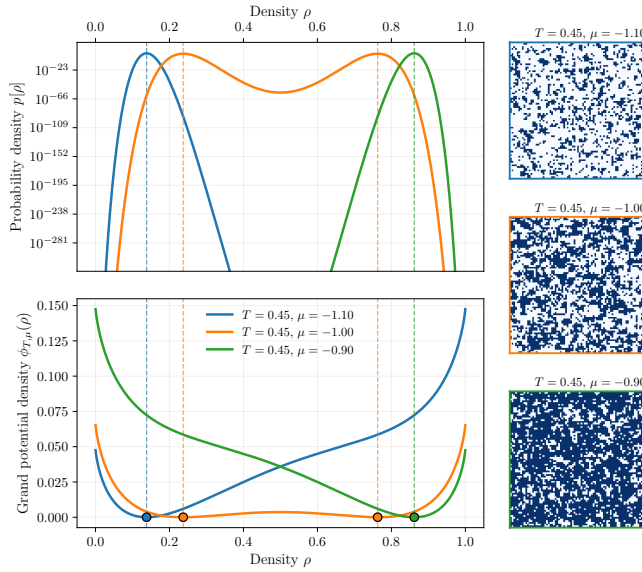


FIG. 3. Interplay of probability and grand potential in the mean-field model ($J = 1.0$). (Top) Probability density $p[\rho]$ as a function of carrier density ρ . (Bottom) The corresponding grand potential landscape, $\phi_{T,\mu}(\rho)$ (shifted vertically for clarity). The peaks in probability correspond directly to the minima in the grand potential. As the chemical potential μ increases, the most probable state (global minimum) shifts from a low-density “vapor” phase (blue) to a high-density “liquid” phase (green), passing through a coexistence point where both phases are equally probable (orange). Insets show representative simulation snapshots for each regime.

state is globally stable; for $\mu > \mu_c$, the high-density state is favored; at $\mu = \mu_c$, both minima have equal depth (coexistence). As μ crosses μ_c , the global minimum of the grand potential jumps discontinuously from the low-density to the high-density state. This jump is the mathematical signature of a first-order phase transition.

D. Connection to device operation

In the lattice-gas description above, the charge carrier population is controlled by the chemical potential μ that appears in the grand-canonical Boltzmann weight of Eq. (1). In the mean-field analysis, this μ enters Eq. (6) as an abstract control parameter that tilts the grand-potential landscape $\phi_{T,\mu}(\rho)$ and thereby selects the most probable carrier density. Sweeping μ along the μ -axis of the phase diagram is equivalent to moving the system across the vapor–liquid phase boundary.

In device operation, this control parameter is set by the electrochemical environment provided by the electrolyte and gate. The electrolyte acts as a reservoir of ions that can exchange charge with the polymer channel, while the gate electrode controls the electrostatic potential of this reservoir relative to the channel. The electrochemical

potential of a charge carrier of charge q is

$$\mu_{\text{ec}} = \mu_{\text{chem}} + q\phi, \quad (9)$$

where μ_{chem} is the chemical contribution and ϕ is the local electrostatic potential. The reservoir (electrolyte plus gate) is characterized by a fixed electrochemical potential, $\mu_{\text{reservoir}}$, and at equilibrium, the electrochemical potential in the channel must match that of the reservoir. Solving for the channel chemical potential that enters the lattice-gas weight gives

$$\mu_{\text{eff}} = \mu_{\text{reservoir}} - q\phi_{\text{ch}}. \quad (10)$$

Only a fraction of the applied gate voltage drops across the channel and couples to the hosting sites, which we capture by a coupling factor $0 < \gamma \leq 1$. At a local channel potential $V_{\text{ch}}(x)$, we approximate the electrostatic potential as $\phi \approx \gamma(V_G - V_{\text{ch}})$, so that the effective chemical potential entering the grand-canonical weight becomes

$$\mu_{\text{eff}}(V_G, V_{\text{ch}}) = \mu_{\text{reservoir}} - \gamma q(V_G - V_{\text{ch}}), \quad (11)$$

where $\gamma = 1$ corresponds to ideal coupling and $\gamma < 1$ accounts for partial screening and voltage division across gate, electrolyte, and channel. In the small-drain-bias limit where $V_{\text{ch}} \approx 0$, this reduces to the simpler form $\mu_{\text{eff}} \approx \mu_{\text{reservoir}} - \gamma q V_G$, making explicit that sweeping V_G is equivalent to sweeping the control parameter μ in Eq. (6).

In the mean-field lattice gas, the occupation ρ of a site with local effective chemical potential μ_{eff} obeys the self-consistency condition (Appendix D)

$$\rho = \frac{1}{1 + \exp\left[-\frac{2J\rho + \mu_{\text{eff}}}{T}\right]}, \quad (12)$$

where J is again the effective mean-field interaction strength and T is the dimensionless temperature. Combining Eqs. (11) and (12) gives the local occupation $\rho(V_G, V_{\text{ch}})$ along the channel for a given gate and drain bias.

To connect this statistical picture to the drain current, we consider a channel of width W , thickness t , and length L biased by a drain voltage V_D . The drain voltage imposes a potential drop $V_{\text{ch}}(x) \in [0, V_D]$ along the channel, so that μ_{eff} and ρ become position dependent. With carrier mobility μ_{tr} and a density of available sites n_{max} , the local conductivity is

$$\sigma(V_G, V_{\text{ch}}) = q \mu_{\text{tr}} n_{\text{max}} \rho(V_G, V_{\text{ch}}). \quad (13)$$

In steady state, the drain current I_D is constant along the channel. Neglecting diffusion and considering only drift transport, the current obeys

$$I_D = -\sigma(V_G, V_{\text{ch}}) W t \frac{dV_{\text{ch}}}{dx}. \quad (14)$$

Eliminating the spatial coordinate x in favour of the channel potential $V_{\text{ch}} \in [0, V_D]$ and integrating yields

$$I_D(V_G, V_D) = -G_0 \int_0^{V_D} \rho(V_G, V_{\text{ch}}) dV_{\text{ch}}, \quad (15)$$

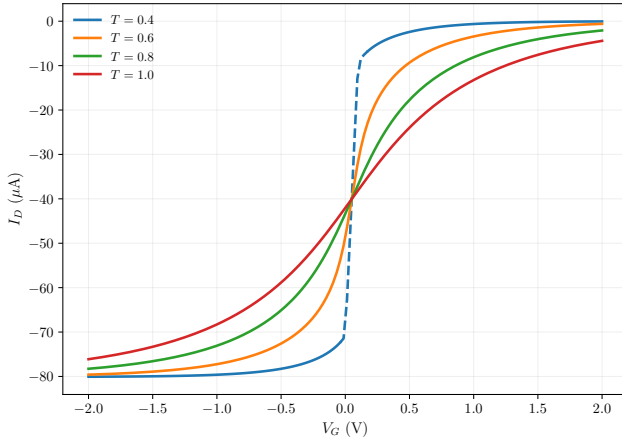


FIG. 4. Predicted transfer characteristics from the lattice-gas model: drain current I_D versus gate voltage V_G at $V_D = 0.1$ V for several reduced temperatures T . Above the critical temperature, the response is smooth; below, the first-order transition produces abrupt switching. Dashed segments indicate where the local chemical potential crosses the coexistence region, corresponding to hysteretic behavior in experiment. Parameters: $J = 1.0$, $\mu_{\text{reservoir}} = -1.0$, $\gamma = 1.0$, $W = 50 \mu\text{m}$, $L = 100 \mu\text{m}$, $t = 100 \text{ nm}$, $n_{\text{max}} = 1 \times 10^{21} \text{ cm}^{-3}$, $\mu_{\text{tr}} = 1 \text{ cm}^2 \text{ V}^{-1} \text{ s}^{-1}$.

where

$$G_0 = \frac{q \mu_{\text{tr}} n_{\text{max}} W t}{L} \quad (16)$$

collects the geometric and kinetic prefactors (Appendix E). Together, Eqs. (6), (11), and (15) provide a link between the grand-canonical description and the measured drain current as a function of gate and drain bias. In the non-interacting limit ($J = 0$), Eq. (15) reduces to a closed expression for $I_D(V_G, V_D)$ obtained by analytic integration of the logistic occupation (Appendix F). In the small-drain limit, $V_D \rightarrow 0$, the channel potential is nearly uniform and $\rho(V_G, V_{\text{ch}}) \approx \rho(V_G, 0)$, so that Eq. (15) simplifies to

$$I_D(V_G, V_D) \simeq -G_0 \rho(V_G, 0) V_D, \quad (17)$$

which is the regime illustrated in Fig. 4, where we plot the drain current I_D as a function of V_G at fixed V_D , assuming typical material and device parameters. Above the critical temperature, the response is smooth and reversible, whereas below, the first-order phase transition produces abrupt switching. In the presence of strong carrier–carrier coupling and slow nucleation dynamics, the system can remain trapped in metastable branches during a gate-voltage sweep, which experimentally manifests as hysteresis between forward and backward traces.

We note that the fundamental control parameter for the metastability is not temperature alone, but the ratio J/T , which encapsulates the balance between energetic and entropic contributions. This is consistent with

experimental reports. For example, Ji et al. reported that OECTs treated with a hydrophobic agent exhibit an increased hysteresis width. In our framework, this treatment enhances coupling by repelling the aqueous solvent, thereby increasing the effective J [25]. Complementary to this, Bongartz et al. reported the inverse trend of shrinking hysteresis with rising temperature [21]. In general, these phenomena are characteristic of OECT systems engineered to be in a ‘strong-coupling’ regime, such as those employing ionic liquids and modified OMC composition, where the ratio J/T is significant.

III. CONCLUSION

We have presented a minimal statistical-mechanics framework based on a lattice gas that describes the quasi-steady state of OMCs in the high charge density regime. Our results demonstrate that phenomena such as phase separation and hysteretic bistability can be understood in analogy to a collective vapor–liquid phase transition, driven by the competition between interaction energy and configurational entropy. The direct connection between gate-voltage sweeps and trajectories through the thermodynamic phase diagram provides a natural explanation for the non-trivial transfer characteristics observed in devices operating in a strong-coupling regime. While this model is a strong simplification of the intricate molecular and electronic landscape of real OMCs, its ability to capture the essential features of a phase transition illustrates the principle of universality: near a critical point, the qualitative macroscopic behavior is governed chiefly by symmetries, dimensionality, and conservation laws rather than microscopic detail.

We close by noting that our mean-field treatment assumes local equilibrium at each point in the channel. A more complete description of spatial inhomogeneities, such as the nanoscale domains observed by Wu et al. [18], would require a Landau–Ginzburg formulation with a gradient term penalizing spatial variations in density. The resulting Cahn–Hilliard dynamics would describe domain coarsening and interface evolution, building naturally on the free energy landscape established here. More broadly, our work suggests that refined descriptions incorporating drift-diffusion transport and explicit spatial structure can be built on the same statistical-mechanical backbone, with J serving as a mesoscopic parameter encapsulating the net effect of underlying microscopic interactions. We aim to pursue these extensions in future work.

ACKNOWLEDGMENTS

The author thanks K. Leo, H. Kleemann, A. Hofacker, and P. Zschoppe for helpful remarks.

Appendix A: Estimate of correlation energies

We perform a simple estimate of the charge carrier interactions in inorganic (silicon) and carbon-based polymer semiconductors. We consider the systems in terms of their three-dimensional charge carrier density n with the average carrier spacing as

$$r \approx n^{-\frac{1}{3}}. \quad (\text{A1})$$

Charge carriers in OMCs are not point-like but possess molecular and polaronic character, residing within an ionic environment. We attempt a rough estimate of the effective carrier–carrier interaction by considering (screened) Coulomb repulsion (E_C) on the one hand, and stabilization through dipole-dipole (E_{dd}), induced dipole (E_{ind}), and lattice relaxation (E_{pol}) interactions on the other, following

$$E_C = \frac{e^2}{4\pi\epsilon_0\epsilon_r} \cdot \frac{1}{r} \cdot \exp\left(-\frac{r}{\lambda_D}\right), \quad (\text{A2})$$

$$E_{dd} = -\frac{2p^2}{4\pi\epsilon_0\epsilon_r} \cdot \frac{1}{r^3}, \quad (\text{A3})$$

$$E_{ind} = -\frac{\alpha e^2}{8\pi\epsilon_0\epsilon_r^2} \cdot \frac{1}{r^4}, \quad \text{and} \quad (\text{A4})$$

$$E_{pol} = -\eta g^2 \hbar\omega_0, \quad (\text{A5})$$

with p the permanent dipole moment, α the polarizability volume, g the dimensionless electron–phonon coupling constant in the Holstein model, and $\hbar\omega_0$ the characteristic phonon energy. The factor $\eta \leq 1$ accounts for the partial overlap of lattice distortions when two polarons share a common relaxation field. In electrochemically doped systems, mobile ions screen the Coulomb repulsion between carriers. We model this through the screening factor in Eq. (A2), with the Debye length

$$\lambda_D = \sqrt{\frac{\epsilon_0\epsilon_r k_B T}{2n_{\text{ion}} e^2}}, \quad (\text{A6})$$

where n_{ion} is the ion concentration in the material. The net effective interaction energy between two carriers is then

$$E_{\text{eff}} = E_C + E_{dd} + E_{ind} + E_{pol}, \quad (\text{A7})$$

with $E_{\text{eff}} > 0$ corresponding to net repulsion and $E_{\text{eff}} < 0$ to net attraction. The dimensionless correlation parameter

$$\Gamma = \frac{E_{\text{eff}}}{k_B T} \quad (\text{A8})$$

quantifies the strength of carrier–carrier interactions relative to thermal fluctuations. For $|\Gamma| \gg 1$, correlations dominate and collective phenomena such as phase transitions become relevant.

Tab. I compares the estimates for both systems using archetypal material parameters. Silicon devices typically

feature carrier densities of $n^{\text{Si}} \sim 10^{16} - 10^{19} \text{ cm}^{-3}$ (moderate to high doping) with $\epsilon_r^{\text{Si}} \approx 12$. Note that in this simple picture, restricting the silicon system to its sheet density in a 2D inversion layer hardly changes the estimated numbers, since carrier spacing remains essentially the same. OMCs, on the other hand, operate in the range of $n^{\text{poly}} \sim 10^{18} - 10^{21} \text{ cm}^{-3}$ with a permittivity of $\epsilon_r^{\text{poly}} \approx 3$ for the ‘dry’ polymer backbone where carriers reside. The estimation suggests that carrier–carrier correlations are significantly stronger in polymer semiconductors than in silicon, and crucially, can be net attractive in nature. This conclusion holds even under strong screening by the electrolytic environment ($\epsilon_r^{\text{poly}} \approx 10$), which changes Γ only marginally. Recent operando X-ray photon correlation spectroscopy measurements on a benchmark OMC have revealed mesoscale phase separation and domain coarsening dynamics consistent with net attractive carrier interactions [18], providing experimental support for this picture.

Appendix B: Mean-field interaction and coexistence chemical potential

1. Mean-field interaction energy

Starting from the lattice-gas Hamiltonian of the main text,

$$H[X] = -J_0 \sum_{\langle i,j \rangle} n_i n_j, \quad (\text{B1})$$

we approximate the interaction energy in terms of the total number of occupied sites $N(X) = \sum_i n_i$.

In the mean-field picture every site is taken to see the average occupation $\rho = N/V$ of all other sites, so that the interaction term for a given site i is approximated as

$$-J_0 \sum_{j \in \text{n.n.}(i)} n_i n_j \approx -\frac{J_0}{2} z \rho n_i, \quad (\text{B2})$$

where z is the coordination number. Summing over all sites gives

$$E(X) \approx -\frac{J_0 z}{2} \rho \sum_i n_i \quad (\text{B3})$$

$$= -\frac{J_0 z}{2} \frac{N(X)}{V} N(X) \quad (\text{B4})$$

$$= -\frac{J_0 z}{2V} N(X)^2. \quad (\text{B5})$$

It is convenient to define a coarse-grained mean-field coupling

$$J \equiv \frac{z}{2} J_0, \quad (\text{B6})$$

so that the interaction energy can be written as

$$E(X) = -\frac{J}{V} N(X)^2. \quad (\text{B7})$$

TABLE I. Order-of-magnitude estimate of charge carrier interactions in silicon and polymer semiconductors ($T = 300\text{ K}$).

$n [\text{cm}^{-3}]$	$r [\text{nm}]$	$E_C [\text{meV}]$	$E_{\text{dd}} [\text{meV}]$	$E_{\text{ind}} [\text{meV}]$	$E_{\text{pol}} [\text{meV}]$	$E_{\text{eff}} [\text{meV}]$	Γ
Si ($\epsilon_r^{\text{Si}} \approx 12$, $\hbar\omega_0 = 60\text{ meV}$, $p = 0\text{ D}$, $\alpha = 5\text{ \AA}^3$, $g = 0.1$, $\eta = 1.0$)							
10^{16}	46.4	2.59	0.00	0.00	-0.6	1.99	0.08
10^{18}	10.0	12.00	0.00	0.00	-0.6	11.40	0.44
10^{19}	4.6	25.85	0.00	0.00	-0.6	25.25	0.98
Polymer ($\epsilon_r^{\text{poly}} \approx 3$, $\hbar\omega_0 = 180\text{ meV}$, $p = 3\text{ D}$, $\alpha = 100\text{ \AA}^3$, $g = 0.9$, $\eta = 0.5$, $n_{\text{ion}} = n$)							
10^{18}	10.0	0.05	0.00	0.00	-72.9	-72.85	-2.82
10^{20}	2.2	0.00	-0.37	-0.37	-72.9	-73.65	-2.85
10^{21}	1.0	0.00	-3.75	-8.00	-72.9	-84.65	-3.27

Inserting this expression into the grand-canonical weight $\mathbb{P}[X] \propto \exp[-(E(X) - \mu N(X))/T]$ used in the main text then yields

$$\mathbb{P}[X] \propto \exp\left[\frac{J}{TV}N(X)^2 + \frac{\mu}{T}N(X)\right]. \quad (\text{B8})$$

2. Mean-field coexistence chemical potential

In this mean-field description, the grand-potential density at temperature T and chemical potential μ can be written as

$$\phi_{T,\mu}(\rho) = -J\rho^2 + T[\rho \ln \rho + (1-\rho) \ln(1-\rho)] - \mu\rho, \quad (\text{B9})$$

where ρ is the carrier density ($0 < \rho < 1$) and $J > 0$ is the effective mean-field attraction defined above.

The coexistence (“critical”) chemical potential μ_c is obtained by exploiting the particle–hole symmetry of the lattice gas. At coexistence, the low- and high-density phases are equally stable, which in mean field corresponds to a symmetry of the grand potential under $\rho \leftrightarrow 1 - \rho$:

$$\phi_{T,\mu_c}(\rho) = \phi_{T,\mu_c}(1 - \rho) \quad \text{for all } \rho. \quad (\text{B10})$$

We therefore consider the difference

$$\Delta\phi(\rho) = \phi_{T,\mu}(\rho) - \phi_{T,\mu}(1 - \rho). \quad (\text{B11})$$

Using Eq. (B9), we obtain

$$\begin{aligned} \Delta\phi(\rho) &= \left[-J\rho^2 - \mu\rho\right] - \left[-J(1-\rho)^2 - \mu(1-\rho)\right] \\ &= -J\rho^2 + J(1-2\rho+\rho^2) - \mu\rho + \mu(1-\rho) \\ &= J(1-2\rho) + \mu(1-2\rho) \\ &= (1-2\rho)(J+\mu). \end{aligned} \quad (\text{B12})$$

The entropic contribution cancels in the difference because $\rho \ln \rho + (1-\rho) \ln(1-\rho)$ is symmetric under $\rho \leftrightarrow 1-\rho$. At coexistence, we require $\Delta\phi(\rho) = 0$ for all ρ , which is only possible if the prefactor of $(1-2\rho)$ vanishes. This yields the mean-field coexistence chemical potential

$$\mu_c = -J. \quad (\text{B13})$$

Appendix C: Derivation of the mean-field entropy

We review the derivation of the entropy term used in the mean-field analysis, which appears in Eq. (6). The goal is to find an analytical expression for the configurational entropy S of a macrostate defined by a carrier density ρ .

The entropy arises from the number of ways, Ω , to arrange $N = \rho V$ indistinguishable charge carriers on a lattice of V distinguishable sites. This is a classic combinatorial problem, and the number of microstates is given by the binomial coefficient:

$$\Omega = \binom{V}{N} = \frac{V!}{N!(V-N)!}. \quad (\text{C1})$$

The configurational entropy is the natural logarithm of this quantity:

$$S = \ln(\Omega) = \ln(V!) - \ln(N!) - \ln((V-N)!). \quad (\text{C2})$$

For a macroscopic system, V , N , and $(V-N)$ are all very large numbers, making the direct computation of the factorials impossible. We can use Stirling’s approximation for the natural logarithm of a factorial, which for large n is given by:

$$\ln(n!) = n \ln(n) - n + O(\ln n), \quad (\text{C3})$$

where $O(\ln n)$ represents terms that grow on the order of $\ln n$. Applying this expression to each term in the entropy equation yields:

$$\begin{aligned} S &\approx (V \ln V - V) - (N \ln N - N) \\ &\quad - ((V-N) \ln(V-N) - (V-N)) \\ &\quad + O(\ln V) - O(\ln N) - O(\ln(V-N)). \end{aligned} \quad (\text{C4})$$

The expression simplifies to:

$$S \approx V \ln V - N \ln N - (V-N) \ln(V-N) + O(\ln V), \quad (\text{C5})$$

where we have combined the logarithmic error terms, as they are all of the same order. We now express N in

terms of the density, so $N = \rho V$:

$$\begin{aligned} S &\approx V \ln V - (\rho V) \ln(\rho V) - (V - \rho V) \ln(V - \rho V) \\ &\quad + O(\ln V) \end{aligned} \quad (\text{C6})$$

$$\begin{aligned} S &\approx V \ln V - \rho V (\ln \rho + \ln V) \\ &\quad - (1 - \rho)V(\ln(1 - \rho) + \ln V) + O(\ln V). \end{aligned} \quad (\text{C7})$$

Expanding and grouping the terms involving $\ln V$:

$$\begin{aligned} S &\approx (V - \rho V - (1 - \rho)V) \ln V \\ &\quad - V(\rho \ln \rho + (1 - \rho) \ln(1 - \rho)) + O(\ln V). \end{aligned} \quad (\text{C8})$$

The prefactor for the leading $\ln V$ term is $V - \rho V - V + \rho V = 0$. This leaves us with the final expression for the entropy:

$$S \approx -V(\rho \ln \rho + (1 - \rho) \ln(1 - \rho)) + O(\ln V). \quad (\text{C9})$$

In the exponent of Eq. (6), this entropy term is combined with the energy term, which scales linearly with V . In the thermodynamic limit ($V \rightarrow \infty$), the $O(\ln V)$ term becomes negligible compared to the leading $O(V)$ terms. We can therefore neglect it to arrive at the entropy density, $s = S/V$:

$$s = \frac{S}{V} \approx -(\rho \ln \rho + (1 - \rho) \ln(1 - \rho)). \quad (\text{C10})$$

This is the standard expression for the entropy of mixing, which forms the entropic part of the mean-field free energy density in Eq. (6).

Appendix D: Mean-field lattice gas and local occupation

In the mean-field lattice-gas description, a site can be either undoped ($n = 0$) or doped ($n = 1$). For a configuration X with $N(X)$ doped sites, the coarse-grained interaction energy is approximated as

$$E(X) = -\frac{J}{V} N(X)^2 - \mu_{\text{eff}} N(X), \quad (\text{D1})$$

where $J > 0$ is the effective mean-field interaction, V is the total number of sites, and μ_{eff} is the effective chemical potential.

Within mean field, each site feels the average occupation $\rho = \langle n_i \rangle = N/V$ of all other sites. The effective single-site internal energy can then be written as

$$E_i(n_i) \approx -(2J\rho + \mu_{\text{eff}}) n_i, \quad (\text{D2})$$

so that the two possible energies are

$$E_i(0) = 0, \quad E_i(1) = -(2J\rho + \mu_{\text{eff}}). \quad (\text{D3})$$

The corresponding single-site grand-canonical partition function is

$$Z_{\text{site}} = \sum_{n_i=0,1} \exp\left[-\frac{E_i(n_i)}{T}\right] = 1 + \exp\left[\frac{2J\rho + \mu_{\text{eff}}}{T}\right], \quad (\text{D4})$$

and the average occupation $\rho = \langle n_i \rangle$ is

$$\rho = \frac{1}{Z_{\text{site}}} \sum_{n_i=0,1} n_i \exp\left[-\frac{E_i(n_i)}{T}\right] = \frac{\exp\left[\frac{2J\rho + \mu_{\text{eff}}}{T}\right]}{1 + \exp\left[\frac{2J\rho + \mu_{\text{eff}}}{T}\right]}. \quad (\text{D5})$$

This can be written in the compact logistic form

$$\rho = \frac{1}{1 + \exp\left[-\frac{2J\rho + \mu_{\text{eff}}}{T}\right]}, \quad (\text{D6})$$

which is the self-consistency condition quoted in Eq. (12) of the main text. Together with the device coupling

$$\mu_{\text{eff}}(V_G, V_{\text{ch}}) = \mu_{\text{reservoir}} - \gamma q(V_G - V_{\text{ch}}), \quad (\text{D7})$$

this defines the local occupation $\rho(V_G, V_{\text{ch}})$ along the channel.

Appendix E: Drift transport and current continuity

We now derive the expression for the drain current. Consider a channel of width W , thickness t , and length L , with coordinate x measured from source ($x = 0$) to drain ($x = L$). The local channel potential is $V_{\text{ch}}(x)$, with boundary conditions $V_{\text{ch}}(0) = 0$ and $V_{\text{ch}}(L) = V_D$. The local carrier density is

$$n(x) = n_{\text{max}} \rho(V_G, V_{\text{ch}}(x)), \quad (\text{E1})$$

where n_{max} is the density of available sites. Assuming drift-dominated transport with mobility μ_{tr} , the local conductivity is

$$\sigma(x) = q \mu_{\text{tr}} n(x) = q \mu_{\text{tr}} n_{\text{max}} \rho(V_G, V_{\text{ch}}(x)). \quad (\text{E2})$$

The current density is $j(x) = \sigma(x)E(x)$ with electric field $E(x) = -dV_{\text{ch}}/dx$. The total drain current I_D is constant along the channel and given by $I_D = j(x)Wt$, so that

$$I_D = -q \mu_{\text{tr}} n_{\text{max}} \rho(V_G, V_{\text{ch}}(x)) Wt \frac{dV_{\text{ch}}}{dx}. \quad (\text{E3})$$

Rearranging yields

$$\frac{dV_{\text{ch}}}{dx} = -\frac{I_D}{q \mu_{\text{tr}} n_{\text{max}} Wt} \frac{1}{\rho(V_G, V_{\text{ch}}(x))}. \quad (\text{E4})$$

Separating variables and integrating from source to drain,

$$\int_0^{V_D} \rho(V_G, V_{\text{ch}}) dV_{\text{ch}} = -\frac{L}{q \mu_{\text{tr}} n_{\text{max}} Wt} I_D, \quad (\text{E5})$$

where we have changed the integration variable from x to V_{ch} , using $V_{\text{ch}}(0) = 0$ and $V_{\text{ch}}(L) = V_D$. This step assumes that $V_{\text{ch}}(x)$ varies continuously and monotonically between source and drain, and that the local carrier density can be written as a single-valued function $\rho(V_G, V_{\text{ch}})$

at fixed V_G (local quasi-equilibrium). These assumptions break down in regimes where the mean-field equation of state becomes multivalued, which would require explicit treatment of domain boundaries and spatial coexistence. We defer this case to future work and restrict our analysis here to the single-phase regime, for which

$$I_D(V_G, V_D) = -G_0 \int_0^{V_D} \rho(V_G, V_{\text{ch}}) dV_{\text{ch}} \quad (\text{E6})$$

with

$$G_0 = \frac{q \mu_{\text{tr}} n_{\text{max}} W t}{L} \quad (\text{E7})$$

as stated in Eq. (15) of the main text.

gistic dependence of the occupation ρ on the effective chemical potential $\mu_{\text{eff}}(V_G, V_{\text{ch}})$ defined in Eq. (D7). Inserting this non-interacting $\rho(V_G, V_{\text{ch}})$ into the integral expression for the drain current, Eq. (E6), yields a closed-form expression for $I_D(V_G, V_D)$. For $J > 0$, Eq. (D6) becomes genuinely non-linear and can admit multiple solutions for ρ at fixed (T, μ_{eff}) . The corresponding grand-potential landscape $\phi_{T, \mu}(\rho)$ develops multiple minima, reflecting the coexistence of low- and high-density phases and giving rise to metastability. In this interacting case, $\rho(V_G, V_{\text{ch}})$ must be obtained self-consistently for each pair (V_G, V_{ch}) , and the drain current $I_D(V_G, V_D)$ in Eq. (E6) has to be evaluated numerically. This is the regime relevant for the phase-separated behavior discussed in the main text.

Appendix F: Non-interacting and interacting limits

In the non-interacting limit ($J = 0$), the mean-field self-consistency relation Eq. (D6) reduces to a simple lo-

- [1] B. D. Paulsen, K. Tybrandt, E. Stavrinidou, and J. Rivnay, *Nature Materials* **19**, 13 (2020).
- [2] P. Gkoupidenis, Y. Zhang, H. Kleemann, H. Ling, F. Santoro, S. Fabiano, A. Salleo, and Y. Van De Burgt, *Nature Reviews Materials* **9**, 134 (2024).
- [3] J. Rivnay, S. Inal, A. Salleo, R. M. Owens, M. Berggren, and G. G. Malliaras, *Nature Reviews Materials* **3**, 17086 (2018).
- [4] Y. Wang, S. Wustoni, J. Surgailis, Y. Zhong, A. Koklu, and S. Inal, *Nature Reviews Materials* **9**, 249 (2024).
- [5] T. He and C. D. Frisbie, *ACS Nano* **16**, 4823 (2022).
- [6] D. H. L. Tjhe, X. Ren, I. E. Jacobs, G. D'Avino, T. B. E. Mustafa, T. G. Marsh, L. Zhang, Y. Fu, A. E. Mansour, A. Opitz, *et al.*, *Nature Materials* **23**, 1712 (2024).
- [7] K. Xu, T.-P. Ruoko, M. Shokrani, D. Scheunemann, H. Abdalla, H. Sun, C.-Y. Yang, Y. Puttison, N. B. Kolhe, J. S. M. Figueiroa, *et al.*, *Advanced Functional Materials* **32**, 2112276 (2022).
- [8] S. Fratini, M. Nikolka, A. Salleo, G. Schweicher, and H. Sirringhaus, *Nature Materials* **19**, 491 (2020).
- [9] S. Ihnatsenka, X. Crispin, and I. V. Zozoulenko, *Physical Review B* **92**, 035201 (2015).
- [10] G. Kim and K. P. Pipe, *Physical Review B* **86**, 085208 (2012).
- [11] R. Warren, P. W. M. Blom, and N. Koch, *Applied Physics Letters* **122**, 152108 (2023).
- [12] K. Ortstein, S. Hutsch, M. Hambach, K. Tvingstedt, B. Wegner, J. Benduhn, J. Kublitski, M. Schwarze, S. Schellhammer, F. Talnack, *et al.*, *Nature Materials* **20**, 1407 (2021).
- [13] N. Vukmirović and L.-W. Wang, *Applied Physics Letters* **97**, 043305 (2010).
- [14] M. Koopmans and L. J. A. Koster, *Applied Physics Letters* **119**, 143301 (2021).
- [15] F. C. Spano and C. Silva, *Annual Review of Physical Chemistry* **65**, 477 (2014).
- [16] M. Koopmans, M. A. T. Leiviskä, J. Liu, J. Dong, L. Qiu, J. C. Hummelen, G. Portale, M. C. Heiber, and L. J. A. Koster, *ACS Applied Materials & Interfaces* **12**, 56222 (2020).
- [17] L. M. Bongartz, G. LeCroy, T. J. Quill, N. Siemons, G. Dijk, A. Marks, C. Cheng, H. Kleemann, K. Leo, and A. Salleo, *Communications Materials* **6**, 241 (2025).
- [18] R. Wu, D. Meli, J. Strzalka, S. Narayanan, Q. Zhang, B. D. Paulsen, J. Rivnay, and C. J. Takacs, *Nature Materials* **23**, 648 (2024).
- [19] P. C. Hohenberg and B. I. Halperin, *Reviews of Modern Physics* **49**, 435 (1977).
- [20] J. W. Cahn and J. E. Hilliard, *The Journal of Chemical Physics* **28**, 258 (1958).
- [21] L. M. Bongartz, R. Kantelberg, T. Meier, R. Hoffmann, C. Matthus, A. Weissbach, M. Cucchi, H. Kleemann, and K. Leo, *Nature Communications* **15**, 6819 (2024).
- [22] R. Ghosh and F. C. Spano, *Accounts of Chemical Research* **53**, 2201 (2020).
- [23] N. Metropolis, A. W. Rosenbluth, M. N. Rosenbluth, A. H. Teller, and E. Teller, *The Journal of Chemical Physics* **21**, 1087 (1953).
- [24] L. M. Bongartz, An interactive lattice gas simulation tool, <https://lukasbongartz.github.io/rust-lattice-simulator/web-deploy/> (2025).
- [25] X. Ji, B. D. Paulsen, G. K. K. Chik, R. Wu, Y. Yin, P. K. L. Chan, and J. Rivnay, *Nature Communications* **12**, 2480 (2021).